Prediction of fuel cell performance degradation using a combined approach of machine learning and impedance spectroscopy

Zewei Lyu [a], Yige Wang [b], Anna Sciazko [a], Hangyue Li [b], Yosuke Komatsu [a], Zaihong Sun [c], Kaihua Sun [c], Naoki Shikazono [a,*], Minfang Han [b,*]

[a] *Institute of Industrial Science, The University of Tokyo, Tokyo 153-8505, Japan*
[b] *Department of Energy and Power Engineering, Tsinghua University, Beijing 100084, China*
[c] *Xuzhou Huatsing Jingkun Energy Co., Ltd., Xuzhou 221005, Jiangsu, China*

ARTICLE INFO

ABSTRACT

Accurate prediction of performance degradation in complex systems such as solid oxide fuel cells is crucial for expediting technological advancements. However, significant challenges still persist due to limited comprehension of degradation mechanisms and difficulties in acquiring in-situ features. In this study, we propose an effective approach that integrates long short-term memory (LSTM) neural network and dynamic electrochemical impedance spectroscopy (DEIS). This integrated approach enables precise prediction of future evolutions in both current-voltage and EIS features using historical testing data, without prior knowledge of degradation mechanisms. For short-term predictions spanning hundreds of hours, our approach achieves a prediction accuracy exceeding 0.99, showcasing promising prospects for diagnostic applications. Additionally, for long-term predictions spanning thousands of hours, we quantitatively determine the significance of each degradation mechanism, which is crucial for enhancing cell durability. Moreover, our proposed approach demonstrates satisfactory predictive ability in both time and frequency domains, offering the potential to reduce EIS testing time by more than half.

1. Introduction

Solid oxide fuel cell (SOFC) has attracted great attention for its high efficiency, fuel adaptability, low emissions, and reversibility [1–3]. In recent years, SOFCs have been preliminarily commercialized in some fields such as 100-kW-level distributed power generation and 1-kW-level residential combined heat and power (CHP). However, further commercialization is hindered by the insufficient lifetime and durability [4,5]. Considerable research efforts have been put in discovering and understanding the complicated degradation mechanisms of cells/stacks during long-term operation [6–8]. Accordingly, durability enhancement methods have been proposed from multiple aspects, including discovery of new functional materials [9,10], micro/macro cell structure engineering [11,12], design of novel stack structures [13,14], reduction of operating temperature [2,3,15], and advanced manufacturing techniques [16,17]. However, as a result of the highly-coupled electrochemical processes, nowadays long-term experiments still remain as the primary means for collecting evidences of degradation behaviors, which are time and resource consuming [18,19].

Performance prediction represents a key methodology to facilitate the commercialization of SOFCs, as it allows scheduling timely maintenance actions, setting application-scenario-related operating conditions, and saving long-term testing costs. Previously, many studies have proposed model-based prediction approaches that account for diverse degradation mechanisms. Depending on the available cell characterization information, different levels of study can be applied into the model formulation and degradation function, including semi-empirical correlations of lumped parameters [20,21], equivalent circuit model (ECM)-based electrical features [22], physics-based time-varying kinetics [23,24], and microstructure information derived from three-dimensional (3D) reconstructions [25,26]. Although these mechanism-specific approaches have shown some predictive success, developing models that describe full cells/stacks operated under practical conditions remains challenging, given the incomplete understanding of

---

the numerous degradation modes and the huge computational cost required for multiscale numerical simulations.

Approaches using data-driven techniques to predict cell performance are attractive and mechanism-agnostic alternatives. Recently, machine learning (ML) has been successfully applied in many fields of SOFCs, including material screening [27], microstructure segmentation and design [28], performance prediction [29], stack structure optimization [30], and fault diagnosis [31]. Regarding degradation effects, so far relatively little attention has been devoted to the development of algorithms for SOFC durability prediction [32–34], but more work has been done in the area of proton exchange membrane fuel cells (PEMFCs) [35]. Direct current (DC) features derived from the discharge curve or polarization curve (IV) are by far the most commonly focused. Compared with the common DC current-voltage data, the electrochemical impedance spectroscopy (EIS), which obtains the impedance over a wide range of Alternating current (AC) perturbation frequencies, is known to contain rich information on all materials properties, interfacial phenomena, and reaction kinetics [36]. EIS has emerged as one such promising in-situ characterization and online monitoring technique that can precisely determine performance changes and degradation rates. Further analysis of the EIS data using the ECM or distribution of relaxation time (DRT) method allows the distinguishment of electrode processes with different time constants [37,38].

Recently, the combination of EIS and ML has shown attractive prospects in many fields of electrochemical energy devices, such as state estimation of lithium-ion batteries [39], fast deconvolution of impedance data [40], multi-condition performance predictions [41,42], diagnostics [43], etc. However, this field of research is still in its infancy and many issues remain unresolved. For example, few studies focus on the time-series forecasting of the entire EIS, which is essential for quantitative degradation analysis. Furthermore, it is unclear whether the research methods/results obtained using laboratory-scale products (such as button cells) can be directly applied into real industrial scenarios. Last but not least, the main drawback of EIS—the high time cost—still restricts its large-scale application and remains to be resolved.

In this work, we develop data-driven models that can accurately predict future short- and long-term evolutions of both IV and EIS using historical testing data, with no prior knowledge of degradation mechanisms. We generated a dataset using a practical industrial-size SOFC for over 5000-h continuous operation with recording 47 IV curves and 188 EIS spectra under 4 different DC biases. For short-term predictions of hundreds of hours, our model can achieve prediction accuracies over 0.99 for both IV and EIS. While for long-term predictions of thousands of hours, by combining the established model with previously proposed dynamic EIS (DEIS) analysis [44], future performance degradation is successfully predicted and quantitatively decoupled. Furthermore, we demonstrate the ability of the proposed model to reduce the time cost of EIS testing. These results illustrate the power of combining data generation with data-driven modelling to predict the behavior of complex systems far into the future.

2. Results and discussion

2.1. Durability testing and data generation

The original data was collected from the durability test of an industrial-size SOFC, as shown in Fig. 1(a). The durability test lasted for 217 days with 10 A DC current load. During cell operation, the EIS (under DC biases of 0, 5, 10, and 30 A) and IV curve were periodically recorded. Note that only the results before Day 156 are shown in Fig. 1, and they were used for the development

of ML models in this study, due to an unexpected thermal cycle occurring on Day 156 (Fig. S1). More details about the experimental measurements can be found in the Methods section.

The recorded IV and EIS (under 5 A DC bias) are shown in Fig. 1 (b–d). The recorded EIS spectra under the other three DC biases are provided in Fig. S2. The gradually steepening IV curve, as well as the increases in ohmic resistance (R_s) and polarization resistance (R_p) indicated by the EIS, evidences the performance degradation during cell operation. Using the recorded EIS spectra, the corresponding DRT results were calculated to distinguish the evolutions of different electrode kinetics. Fig. 1(e) displays the DRT evolution under 5 A DC bias. The DRT results under the other three DC biases are also provided in Fig. S2. Typically, for the cell structure employed in this study, five characteristic peaks can be distinguished in a single DRT plot, which correspond to following electrode kinetics based on our experimental verifications (Fig. S3 for details).

(1) P_{A1} and P_{A2} are ascribed to anode charge transfer reactions and ionic transport close to three phase boundaries (TPB).
(2) P_{C1} (partially overlapped with P_{A3}) is associated with O_2 surface exchange kinetics as well as the O^{2-} diffusion.
(3) P_{A3} is related to gas-phase diffusion and gas conversion at the anode.
(4) P_{C2} is caused by gas-phase diffusion at the thin cathode which is negligible when air is used as oxidant.

During cell operation, P_{A2} increased most significantly, reflecting the attenuation of anode charge transfer reactions. Meanwhile, the two peaks corresponding to P_{C1} and P_{A3} also increased visibly. However, due to the partial overlap of these two processes, we cannot accurately distinguish them solely through DRT. In addition, DRT can only provide qualitative distinguishment of different electrode processes. It is not possible to directly correlate the growth of DRT peaks with the voltage degradation depicted in Fig. 1(a). In our previous work [44], the contributions of different electrode processes to the voltage degradation were quantitatively determined based on DEIS measurements and analysis. However, this method relies on numerous EIS measurements, which are time-consuming and costly in practice.

Therefore, in this study, we validated a ML model based on long short-term memory (LSTM) network—which is thought to be one of the most advanced networks to process temporal sequences [45]—using the dataset before Day 156. Specifically, two predictive models were established and validated—one for predicting EIS and the other for predicting IV. Afterwards, we used the validated models to predict the EIS spectra and IV curves up to Day 217. By employing the predicted DEIS spectra, we quantitatively decoupled the voltage degradation from Day 20 to Day 217. Furthermore, we demonstrated the ability of LSTM-based model to expedite EIS testing, providing practical benefits for the implementation of the proposed methodology.

2.2. Formulation of LSTM-based neural networks

The collected EIS dataset includes 5 dimensions: [**Frequency**, **Zre**, **Zim**, **Time**, **DC bias**]. While the IV dataset includes 3 dimensions: [**Current**, **Voltage**, **Time**]. Before feeding the EIS and IV datasets into the LSTM-based neural networks, they should be formatted as sequential types. When constructing EIS sequences, **Frequency**, **Time**, and **DC bias** are used as inputs, while real and imaginary pats of impedance (**Zre** and **Zim**) are used as outputs. It should be noted that the direction of the input sequence can be selected from different input dimensions, which may result in different mechanisms for the LSTM unit to generate memory,
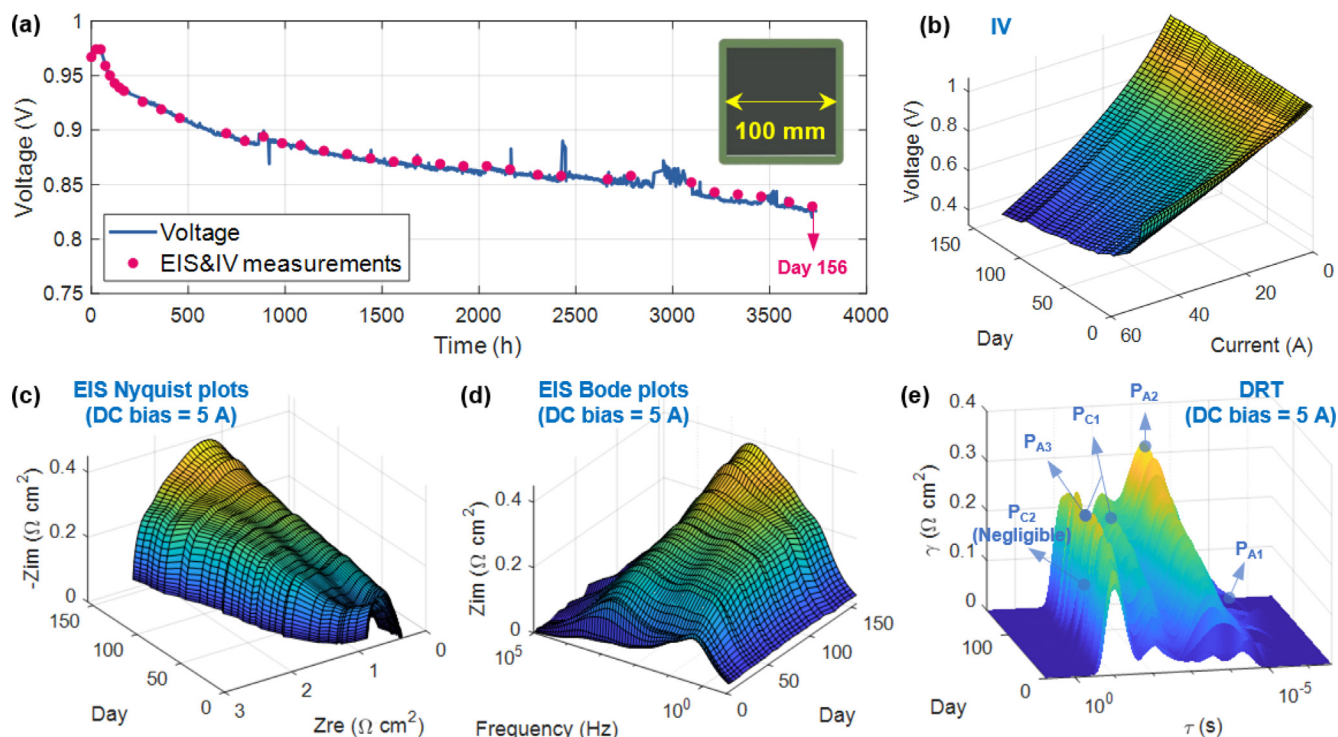
Fig. 1. Temporal evolution patterns of the electrochemical characteristics of the fuel cell. (a) Time change of voltage during the galvanostatic durability test, where EIS and IV measurement dates are marked as red dots, and the marked voltage values are derived from the voltage corresponding to 10 A current in (b) the recorded IV curves. The recorded EIS spectra under 5 A DC bias: (c) Nyquist plots, (d) Bode plots, and (e) the corresponding DRT results. The full day list of EIS & IV measurements is provided in Table S1. The measurement results after Day 156 are provided in Figs. S1 and S2, but note that they were not used for model development.

thereby affecting the prediction results. The main differences are described as:

(1) For frequency-direction LSTM (Fig. 2a), **Frequency** serves as the direction of the input sequences, while **Time** and **DC bias** serve as labels, which are fixed in a single input sequence. In the following, this configuration is referred to as 'F-LSTM'.

(2) For time-direction LSTM (Fig. 2b), **Time** serves as the direction of the input sequences, while **Frequency** and **DC bias** serve as labels and are fixed in a single input sequence. This configuration is referred to as 'T-LSTM'.

(3) In principle, **DC bias** can also serve as the direction of the input sequences. However, due to the small number of DC biases—only 4 in this case—the sequence length is too short for LSTM to generate memory. Therefore, only F-LSTM and T-LSTM are used and compared for EIS predictions.

When constructing IV sequences, **Time** and **Current** are used as inputs, while the corresponding **Voltage** is used as an output. Similar to EIS-LSTM, the configurations of IV-LSTM include current-direction LSTM (referred to as 'C-LSTM') and time-direction LSTM (referred to as 'T-LSTM'), which are illustrated in Fig. S4.

The predictive performances of the two EIS-LSTM configurations—F-LSTM and T-LSTM—are compared in Table 1, which are quantified using the coefficient of determination (R^2) on the test set. More details on the network structure can be found in the Methods section. By comparison, the F-LSTM exhibits better performance in both Zre and Zim predictions. Although the T-LSTM has slightly better prediction accuracy for Zre under lower proportion of train set (0.6 and 0.7), its prediction accuracy for Zim is unacceptable (<0.75). In addition, the standard deviations of F-LSTM are visibly lower than those of T-LSTM, indicating that the robustness of the former is better. Therefore, it is speculated that

LSTM is good at capturing the impact of frequency on impedance through its intrinsic memory mechanism. However, if frequency serves as the label rather than the input direction, its impact can hardly be learned adequately—especially for Zim, since it is strongly non-monotonic with frequency.

As for the IV predictions, the T-LSTM exhibits significantly better performance and robustness than the C-LSTM, as shown in Table 2. Therefore, compared to current, the effect of time on voltage is more easily captured by the intrinsic memory mechanism of LSTM. By using current as a label, it is sufficient to impose appropriate influence of the current on network memory.

Therefore, in the following, F-LSTM was adopted for EIS prediction tasks, and T-LSTM was adopted for IV prediction tasks.

2.3. Predictions of fuel cell performance

Data efficiencies of the F-LSTM (for EIS predictions) and the T-LSTM (for IV predictions) are evaluated in Fig. S5. Finally, the data from Day 1 to Day 145 were used as the training set (i.e. n (training) = 0.95), while the remaining data on Day 151 and Day 156 were used as the test set (Table S1). After being validated on the test set, the models were then used to predict the future cell performance up to Day 217. Fig. 3(a and b) shows the predictions of IV and EIS (under 5 A DC bias), respectively. EIS predictions under the other three DC biases are provided in Fig. S6. As shown in Fig. 3 (d–f), the prediction accuracy of voltage, Zre, and Zim quantified by R^2 all exceeds 0.99 for the test set, which verifies the effectiveness of the models for short-term predictions. The effectiveness for long-term predictions is examined in the next section.

We then used the predicted EIS spectra for DRT calculations. Before doing so, it is essential to verify the physical rationality of the predicted EIS through the Kramers-Kronig (K-K) test [46], as shown in Fig. S7. The residuals of the predicted EIS increase with
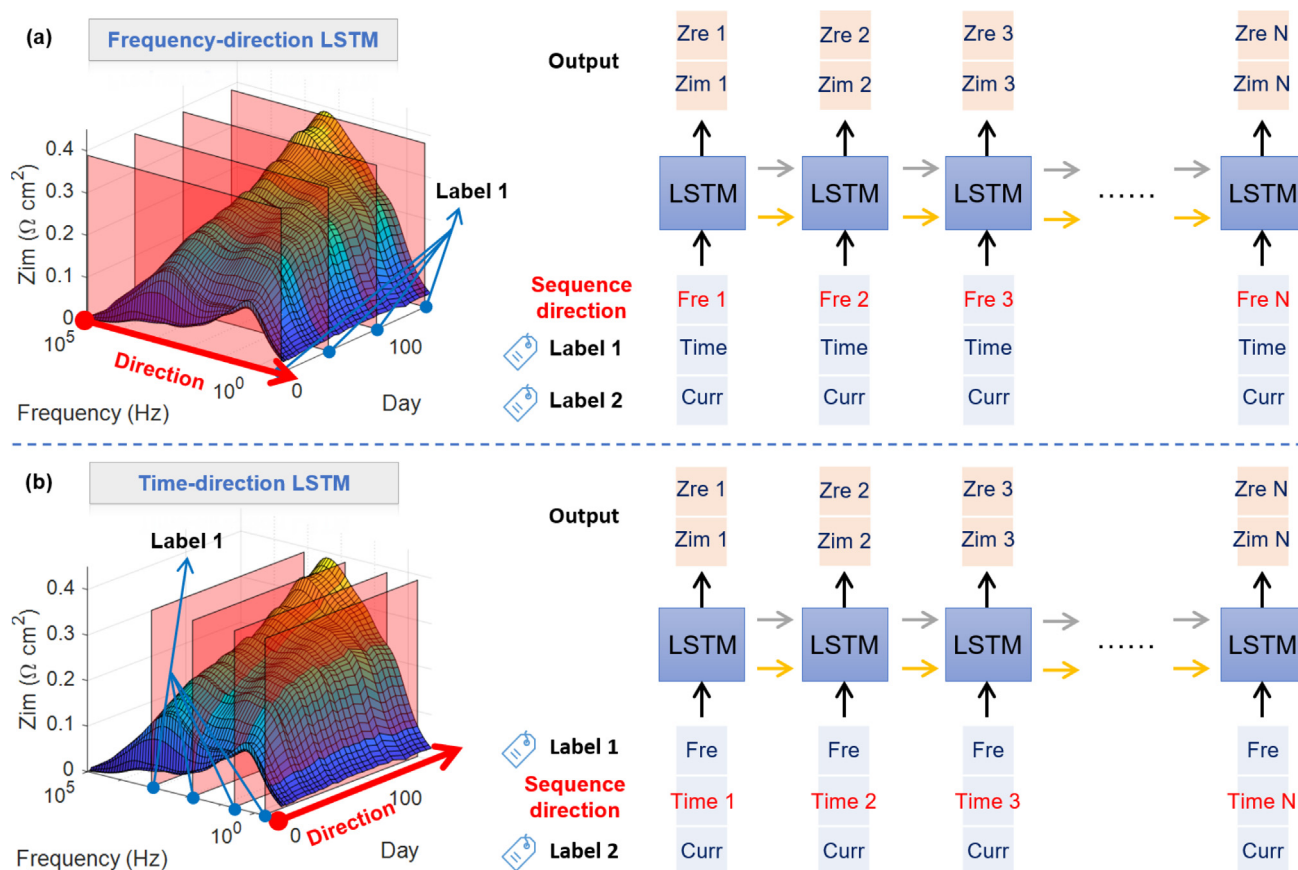
Fig. 2. Two different LSTM configurations for EIS predictions. (a) Frequency-direction LSTM (F-LSTM) and (b) Time-direction LSTM (T-LSTM). Three-dimensional surfaces on the left show the temporal evolution of the measured EIS Bode plots. The 'Sequence direction' and corresponding 'Label 1' are illustrated in the figure. The intersection lines between the red planes and the Bode surface indicate different Zim sequences.

Table 1
Predictive performance of the F-LSTM and the T-LSTM in predicting EIS.

n (training) [a]	0.6		0.7		0.8		0.9	
F-LSTM	R^2 (Zre)	R^2 (Zim)	R^2 (Zre)	R^2 (Zim)	R^2 (Zre)	R^2 (Zim)	R^2 (Zre)	R^2 (Zim)
	0.9319[b]	0.8858	0.9431	0.9180	0.9938	0.9745	0.9883	0.9831
	Std (Zre)	Std (Zim)	Std (Zre)	Std (Zim)	Std (Zre)	Std (Zim)	Std (Zre)	Std (Zim)
	0.0159[c]	0.0191	0.0074	0.0109	0.0026	0.0046	0.0017	0.0022
T-LSTM	R^2 (Zre)	R^2 (Zim)	R^2 (Zre)	R^2 (Zim)	R^2 (Zre)	R^2 (Zim)	R^2 (Zre)	R^2 (Zim)
	0.9687	0.4461	0.9736	0.7366	0.9643	0.9705	0.9788	0.9549
	Std (Zre)	Std (Zim)	Std (Zre)	Std (Zim)	Std (Zre)	Std (Zim)	Std (Zre)	Std (Zim)
	0.0181	0.2099	0.0090	0.1056	0.0094	0.0105	0.0042	0.0074

[a] '*n* (training)' indicates the proportion of training set.
[b] 'R^2' indicates an average value over 10 different random initializations.
[c] 'Std' indicates the standard deviation of R^2 over 10 different random initializations.

the extension of predicted time, especially in the high-frequency range. Therefore, the future predictable days are limited by the physical rationality of EIS predictions. The DRT calculation results using the predicted EIS spectra (under 5 A DC bias) are shown in Fig. 3(c). The results under the other three DC biases are provided in Fig. S6. The prediction accuracy of DRT (Fig. 3g–j) is visibly worse than that of EIS (Fig. 3e and f). This is reasonable because the numerical calculation of DRT is very sensitive to small deviations and noises in the EIS [40,47]. Detailed comparisons of the predicted and measured results of EIS and DRT in the test set are provided in Figs. S8 and S9. The DRT predictions can basically reproduce the peak shapes of the measured results. Besides, with the increase in DC bias, more satisfactory prediction accuracy of DRT can be obtained. Considering that DRT calculations are only

used for preliminary analysis and to provide initial values for the subsequent ECM fittings, we believe that such prediction accuracy is acceptable.

In the future, it may be possible to establish LSTM-based neural networks to directly predict DRT. But naturally, this comes with additional computational time and costs. We defer consideration of those aspects to future work.

2.4. Decoupling of performance degradation

Subsequently, we decoupled the voltage degradation from Day 20 to Day 217 using the predicted EIS and IV, based on the previously established DEIS method [44]. Time course of the predicted voltage at 10 A current was extracted from the predicted IV curves,

Table 2
Predictive performance of the C-LSTM and the T-LSTM in predicting IV.

n (training)[a]	0.6	0.7	0.8	0.9
C-LSTM	R^2	R^2	R^2	R^2
	0.9155[b]	0.9176	0.9802	0.9916
	Std	**Std**	**Std**	**Std**
	0.0106[c]	0.0164	0.0039	0.0016
T-LSTM	R^2	R^2	R^2	R^2
	0.9713	0.9933	0.9972	0.9980
	Std	**Std**	**Std**	**Std**
	0.0171	0.0055	0.0006	0.0005

^a '*n* (training)' indicates the proportion of training set.
^b 'R^2' indicates an average value over 10 different random initializations.
^c 'Std' indicates the standard deviation of R^2 over 10 different random initializations.

[a] '*n* (training)' indicates the proportion of training set.
[b] 'R^2' indicates an average value over 10 different random initializations.
[c] 'Std' indicates the standard deviation of R^2 over 10 different random initializations.
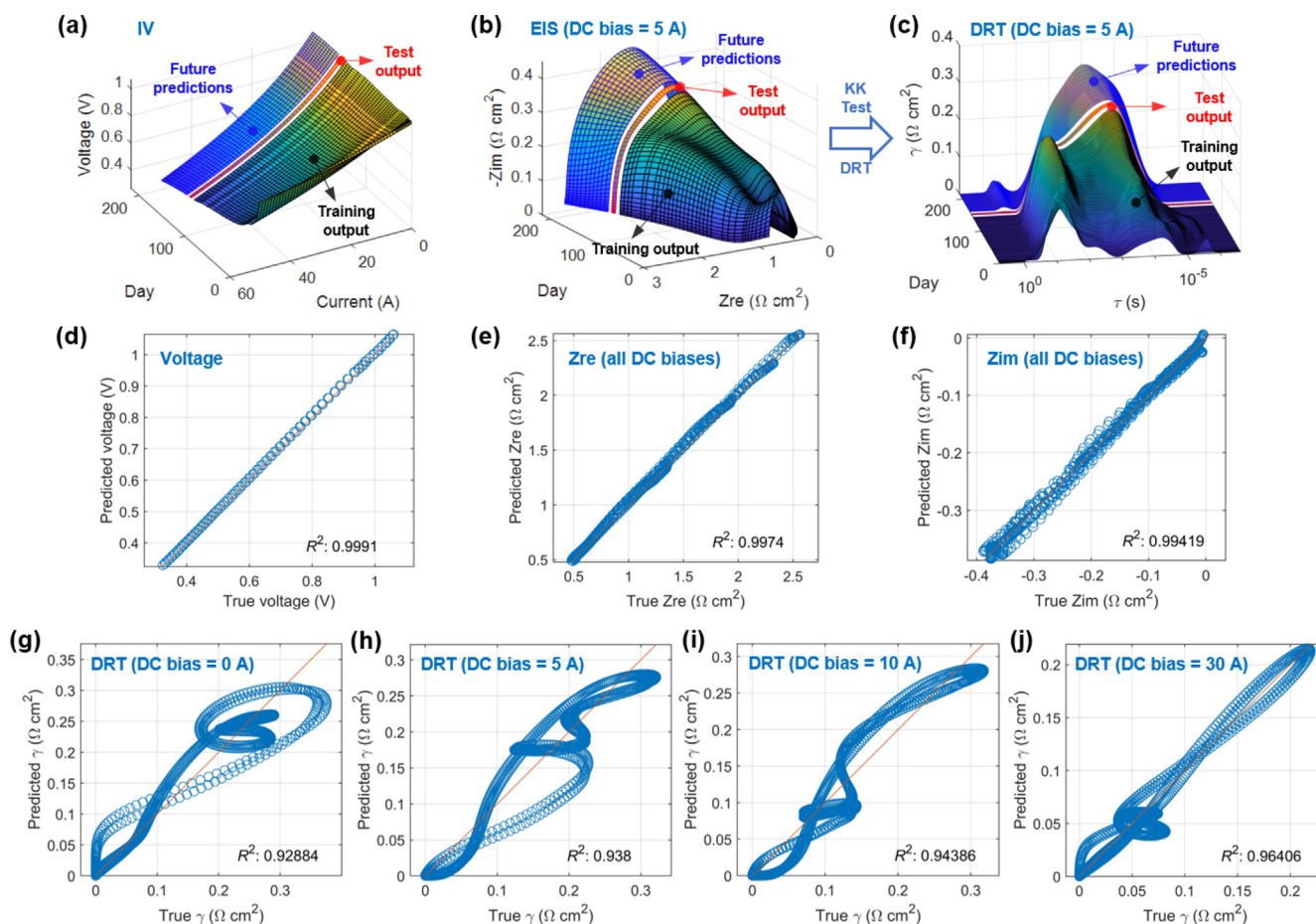
Fig. 3. Predictions of the cell performance using LSTM-based neural networks. Predictions of (a) IV curves, (b) EIS spectra under 5 A DC bias, and (c) corresponding DRT calculation results. The EIS and DRT predictions under the other three DC biases are provided in Fig. S6. Evaluations on the prediction accuracies (on the test set) of (d) voltage, (e) Zre, (f) Zim, and DRT under DC biases of (g) 0 A, (h) 5 A, (i) 10 A, and (j) 30 A.

as shown in Fig. S10. From Day 20 to Day 217, the predicted voltage decreased from 0.917 to 0.818 V, indicating a voltage degradation of 99 mV. While in actual testing, the measured voltage on Day 217 was lower than 0.8 V (Fig. S1a). This difference is reasonable, considering that the unexpected thermal cycle occurred on Day 156 may accelerate later performance degradation.

It should be noted that in addition to the initially selected 4 DC biases—0, 5, 10, and 30 A—we also used the LSTM model to predict the EIS spectra under the other 8 DC biases—1–4 A and 6–9 A (with 1 A interval), as shown in Fig. S11. These predictions are beneficial

for the data abundance when conducting impedance-based degradation analysis.

The method of decoupling the voltage degradation mainly includes 4 steps: EIS collection, DRT calculation, ECM fitting, and overpotential calculation. More details on each step can be found in the Methods section. According to the five electrode processes identified through DRT analysis, an ECM consisting of an ohmic resistor, an inductor, four R//CPE elements, and a Gerischer element is used to fit the EIS data, as shown in Fig. 4(a). The subscripts of ECM components correspond to the subscripts of DRT peaks
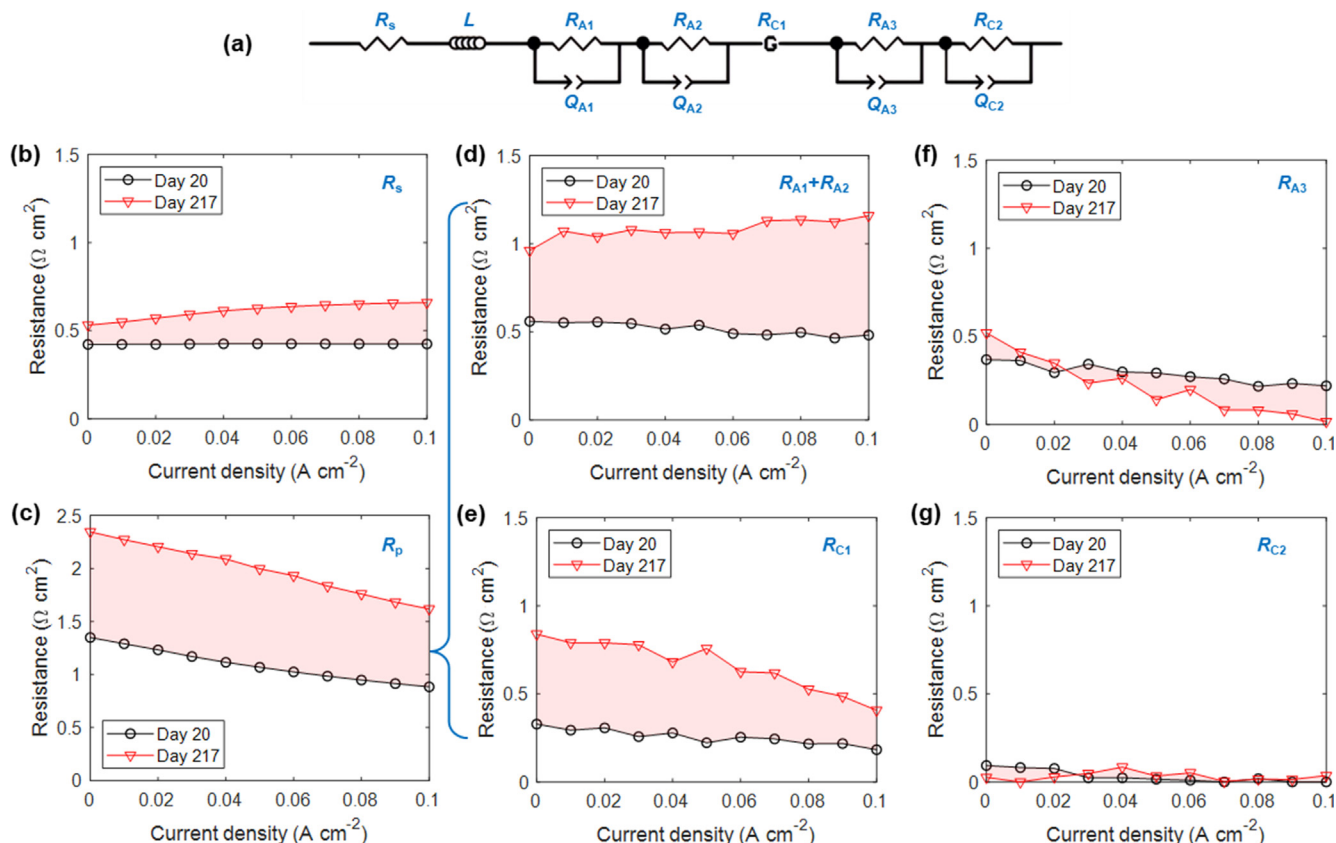
Fig. 4. ECM fitting results of the predicted EIS spectra on Day 20 and Day 217. (a) The ECM used in this study. Fitted values of the resistances under varied DC biases: (b) R_s, (c) R_p, (d) $R_{A1} + R_{A2}$, (e) R_{C1}, (f) R_{A3}, and (g) R_{C2}. The red shaded area indicates the corresponding resistance-induced overpotential growth from Day 20 to Day 217. It should be noted that when the Day 217 curve is above, the area value is positive, while when the Day 20 curve is above, the area value is negative.

shown in Fig. 1(e). The ECM fitting results are shown in Fig. 4(b–g), and the fitting residuals are plotted in Figs. S12 and S13 for Day 20 and Day 217, respectively. The fitting residuals at most frequencies are within ±5%, ensuring the rationality and reliability of the fitting results. As a result, in Fig. 4(b–g), the area of the red region in each graph represents the corresponding resistance-induced overpotential growth from Day 20 to Day 217—in other words, its contribution to the voltage degradation.

For clear comparison, the percentage contributions of different processes to the total voltage degradation are calculated, which are shown in Fig. 5(a). Some key findings are as follows:

(1) The sum of deteriorations of P_{A1} & P_{A2} dominates the overall performance degradation, and its contribution rate is 51.9%. As previously reported, the main degradation mechanisms of Ni-YSZ anode are Ni coarsening and migration (Fig. 5c), which may cause the decrease in effective TPB length in the anode [7,8,23,25,26].

(2) The second largest contribution comes from P_{C1} with a contribution rate of 37.8%. The main degradation mechanisms of the LSCF cathode are its chemical reactions with gaseous components and adjacent cell layers, such as Cr poisoning and Sr segregation (Fig. 5d), which may lead to the decrease in its catalytic activity [6,7,17,48].

(3) Thirdly, the contribution rate of P_s is 17.3%. The main reasons for the increase in ohmic resistance include external factors—oxidation of stack components such as interconnectors and contact materials [6,18]; and internal factors—

phase transition of the YSZ electrolyte [49], and for the anode-supported cells, Ni coarsening and migration can also affect the ohmic resistance [8].

(4) The contribution of P_{A3} is slightly negative, indicating that the anode gas-phase diffusion and conversion were somewhat enhanced. This phenomenon is consistent with our previous reports [44]. It is mainly due to the increased anode porosity caused by Ni agglomeration.

(5) The contribution of P_{C2} is minimal. This is reasonable, considering that for anode-supported cells, the overpotential due to gas-phase diffusion at the cathode is negligible [37].

Note that all of the above degradation mechanisms have been reported in the literature. However, for the first time, the importance of each mechanism in long-term operation—which is very important for improving cell durability—was quantitatively determined here. It should be mentioned that the decoupling results of the voltage degradation depend on the specific information of the cell, such as materials, structures, operating conditions, etc. However, the proposed decoupling method is universal.

For verification, following the same method, the voltage degradation from Day 20 to Day 217 was also decoupled using the measured EIS spectra. The ECM fitting results of the measured EIS are provided in Fig. S14, and the decoupling results of the voltage degradation are shown in Fig. 5(b). Compared with the results in Fig. 5(a), the main differences are the larger contributions of P_{A1} & P_{A2} and P_s in Fig. 5(b), which should be caused by the unexpected thermal cycling occurring on Day 156. However, the contribution of each process to the total voltage degradation is in the same order, i.e., P_{A1} & P_{A2} > P_{C1} > P_s > P_{C2} > P_{A3}. This verifies the effective-
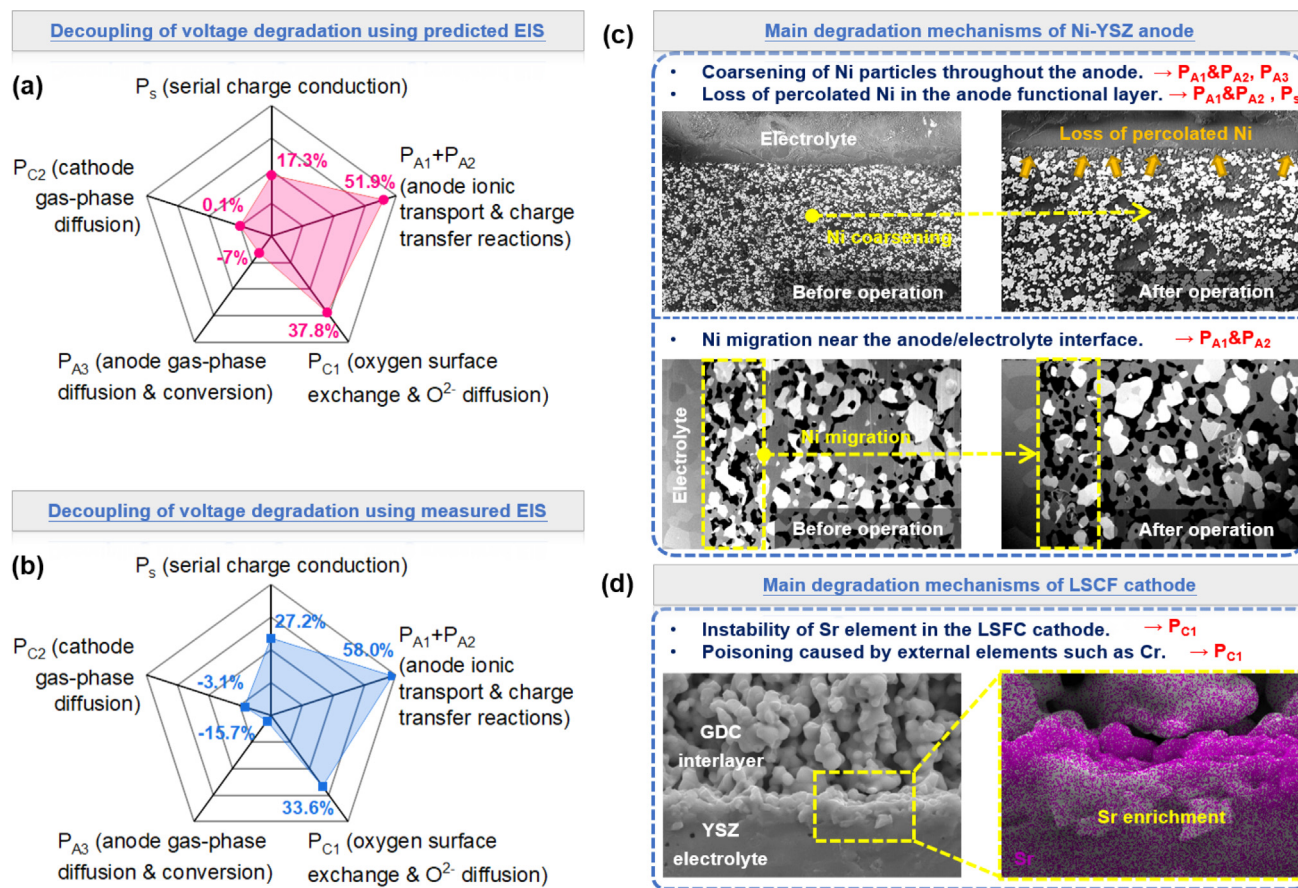
Fig. 5. Decoupling results of the voltage degradation from Day 20 to Day 217 and the underlying dominant degradation mechanisms. Percentage contributions of different processes to the total voltage degradation determined using (a) predicted EIS spectra and (b) measured EIS spectra. The underlying dominant degradation mechanisms of (c) Ni-YSZ anode and (d) LSCF cathode. The red arrows indicate the electrode processes affected by each mechanism. These microstructural photographs are from post-characterizations of the same batch of cells used in this study. For more details, refer to our previous works [44,50].

ness of the models for long-term predictions and the reliability of the decoupling method to a certain extent.

2.5. Reducing the time cost of EIS testing

In the above sections, we demonstrate the combination of LSTM-based neural networks and DEIS analysis to predict and decouple the performance degradation of an industrial-sized SOFC. However, inherently high time cost of EIS measurements may limit the practical application of this method. Although we can predict EIS spectra under more DC biases than actual measurements (Fig. S11), we consider it is not enough to fully overcome the above difficulty. We recorded the test duration of a typical EIS measurement, as shown in Fig. 6(a). The total test duration is 710 s, of which the duration at the first 6 high-frequency decades only accounts for 25.5%. However, the last one low-frequency decade accounts for the most—74.5%. Therefore, the key to shortening the EIS test duration is to accelerate the acquisition of low-frequency impedances.

A possible solution is to use LSTM-based neural networks to predict the low-frequency impedances instead of measuring them. As shown in Fig. 6(b), we masked a portion of the low-frequency impedances in the training set to simulate the absence of low-frequency measurements. While in the test set, the impedances at all frequencies need to be predicted. Compared with the situation in Fig. 3(b), the current task poses more challenges to the predictive ability of the model in the frequency domain. We compared the prediction accuracy under different low-frequency exposure

days in the training set, as shown in Fig. 6(c). When the low-frequency impedances in the training set are completely masked, although the high-frequency impedances are predicted well, the prediction accuracy of the low-frequency Zim is unacceptable. However, by exposing some of the low-frequency impedances in the training set—even for just one day—the predictions of low-frequency Zim can be significantly improved. This is reasonable because the exposure of low-frequency impedances provides more information for the model to learn the low-frequency characteristics of EIS. However, further increasing the exposure days does not seem to be effective in improving the prediction accuracy, which is limited by the intrinsic capability of the model. Detailed predictions of the EIS spectra in the test set are presented in Figs. S15 and S16 for Day 151 and Day 156, respectively. And their K-K test residuals are plotted in Figs. S17 and S18, respectively. Clearly, by exposing some of the low-frequency impedances in the training set, the prediction accuracy and physical rationality of the EIS predictions can be significantly improved.

Therefore, we only need to test the time-consuming low-frequency impedances on a few days, while on most days, only the fast high-frequency impedances need to be measured. By using LSTM-based neural networks, the future low-frequency impedances can be well predicted. In this way, the time cost of EIS testing can be almost halved.
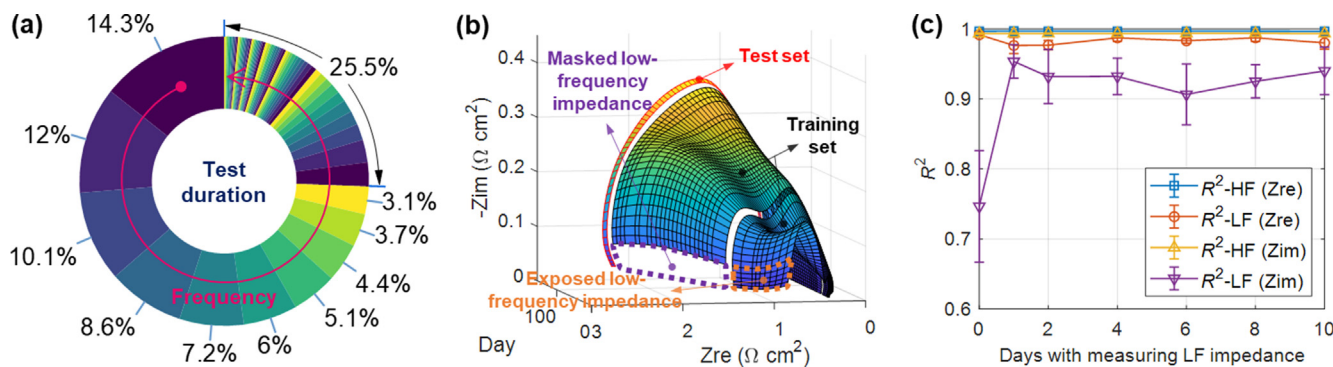
Fig. 6. Reducing the time cost of EIS testing by LSTM predictions. (a) Test durations at different frequencies in a typical EIS measurement. Raw data are provided in Table S2. (b) Illustration of masking and exposure of low-frequency impedances in the training set. The low frequency impedances here are defined as the impedances at the lowest 5 frequencies, i.e., 0.43089, 0.35566, 0.29356, 0.24231, and 0.20000 Hz. The data from Day 1 to Day 145 are used as the training set, and the data on Day 151 and Day 156 are used as the test set. (c) Prediction accuracies with different low-frequency exposure days in the training set. The prediction accuracy is quantified using R^2, which is calculated and plotted for the high-frequency Zre, low-frequency Zre, high-frequency Zim, and low-frequency Zim, respectively. The F-LSTM was used for EIS predictions here.

2.6. Outlook and discussion

The results of this study demonstrate that the proposed LSTM-based neural network can reasonably predict future performance degradation using historical testing data. Furthermore, future performance degradation can be quantitatively decoupled by combining the DEIS-based analysis method. Although the cell used here was subjected to a galvanostatic durability test, it should be noted that the proposed prediction approach is not restricted to a single operating condition. It holds the potential to forecast the evolutions of IV and EIS under more complex conditions, such as reversible cycles (RSOC), current load cycles, and thermal cycles.

Furthermore, the proposed approach has broader applications in aging studies of various electrochemical energy devices. For instance, EIS has already demonstrated successful application in assessing and predicting battery states due to its rich information content, encompassing properties like State of Charge (SOC) and State of Health (SOH) during battery aging [39,51]. By integrating the EIS prediction method proposed in this study, future battery state information can be readily obtained without the need for extensive aging tests. Moreover, EIS analysis techniques like DRT and ECM have garnered significant attention within the battery community [52,53], thereby paving the way for the potential implementation of the proposed degradation analysis method in batteries.

Lastly, this study essentially showcases the time-series prediction of electrochemical properties (e.g., IV and EIS) based on historical data. These properties can be one-dimensional or multi-dimensional. In the future, time-series predictions of more electrochemical or other types of properties (e.g., electrode microstructures) can be explored. Advanced machine learning methods for time-series forecasting can be adopted and improved accordingly.

3. Methods

3.1. Fuel cell fabrication

The commercially available SOFC used in this study consists of Ni-YSZ (8 mol% Y_2O_3-stabilized ZrO_2) anode support (AS), Ni-YSZ anode functional layer (AFL), YSZ electrolyte, GDC ($Gd_{0.1}Ce_{0.9}O_{2−\delta}$) interlayer, and LSCF ($La_{0.6}Sr_{0.4}Co_{0.2}Fe_{0.8}O_{3−\delta}$) cathode [50]. The AS was firstly prepared by tape casting, and then the AFL and the electrolyte were prepared by screen printing in turn on the dry AS. The prepared half-cell was then sintered at 1350 °C for 10 h to densify the electrolyte. Afterwards, the GDC interlayer was screen-printed on the half-cell and then sintered at 1300 °C for 5 h. Finally, the

LSCF cathode was screen-printed and sintered at 1100 °C. The cross-sectional micromorphology of the cell is shown in Fig. S19. The thickness of AS, AFL, electrolyte, interlayer, and cathode are about 600–650, 5–10, 10–15, 5–10, and 25–30 μm, respectively. The overall size of the cell is 124 × 124 mm², while the electrochemically active area determined by the cathode size is 100 × 100 mm², as shown in Fig. 1(a).

3.2. Electrochemical measurements

A single cell testing device was manufactured to characterize the electrochemical performance of the cell, as shown in Fig. S20. The cell was sandwiched between two end plates (interconnectors). LSCF and NiO slurries were used as contact materials for cathode and anode, respectively. Silver meshes were used as current collectors. Alumina-based ceramic adhesive (Zhuzhou Spring Polymer SL8308) was used for sealing. Two silver rods were used to export the electronic current, while two silver wires were used to measure the voltage. The cell was processed and operated at 720 °C. During the operation, 1 L min⁻¹ of H_2 mixed with 0.1 L min⁻¹ H_2O was provided to the anode and 3 L min⁻¹ of air to the cathode. The measured electrochemical characteristics include:

(1) IV curve. The measurement was started from open circuit (OC). Then, the electrical current controlled by an electronic load (Itech IT8514C +) was stepwise increased (1 A per step). A dwell of 10 s was predefined at each electrical current to ensure a steady state before recording the voltage.
(2) EIS. In this study, EIS spectra under 4 different DC biases (0, 5, 10, and 30 A) were measured. During testing, the AC and DC signals were controlled by an electrochemical workstation (Zahner IM6) and an electronic load, respectively. A special screen circuit was designed to avoid the influence of AC signals on the electronic load. The frequency range for EIS testing is from 100 kHz to 0.2 Hz (Table S2), and the AC amplitude is 1 A.
(3) Galvanostatic durability. The durability test lasted for 217 days with 10 A DC current load. The EIS (under DC biases of 0, 5, 10, and 30 A) and IV were recorded on 47 days throughout the durability test. The full day list of EIS & IV measurements is provided in Table S1.

3.3. Data processing for machine learning

In practice, EIS testing is often subject to inevitable interference such as inductance and fluctuations, while machine learning meth-

ods may be sensitive to data noise. Therefore, the original EIS spectra were modified and smoothed using our previously proposed algorithm based on the weighted K-K test [47]. The original EIS spectra and the processed ones are shown in Figs. S21 and S22, respectively.

The collected EIS dataset includes 5 dimensions:

[log(Frequency), Zre, Zim, Time, DC bias].

Note that the frequency data were logarithmic during processing. While the IV dataset includes 3 dimensions:

[Current, Voltage, Time].

All dimensions were normalized to the distribution with zero mean and unit variance to diminish the influence of different data scales.

3.4. Machine learning approach

In this study, a LSTM-based neural network was constructed, whose structure and parameters are shown in Fig. S23 and Table S3, respectively. This network consists of two layers of LSTM and a fully connected layer. To prevent overfitting, two dropout layers are inserted between them. The dataset (collected before Day 156) was divided into two sections, referred to as the training and test sets. The training set was used to fit the hyper-parameters and determine the values of the coefficients. The test set was then used as a measure of network performance. The dataset from Day 161 to Day 217 was not used for network development, because the cell performance changed drastically on Day 161 due to an unexpected thermal cycle (Figs. S1 and S2). However, we also used the validated network to predict cell performance from Day 161 to Day 217, referred to as future predictions. Based on the predicted EIS and IV, the performance degradation from Day 20 to Day 217 was analyzed in detail. The analysis results were compared with the test results to speculate the impact of the unexpected thermal cycle on later performance degradation mechanisms.

In most cases, the coefficient of determination (R^2) in the test set was used to evaluate the network performance, which is defined as:

$$R^2 = 1 - \frac{\sum_{i=1}^{n}\left(y_i^{\text{Pred}} - y_i^{\text{Meas}}\right)^2}{\sum_{i=1}^{n}\left(y_i^{\text{Meas}} - \bar{y}^{\text{Meas}}\right)^2}$$

where y_i^{Pred} is the predicted value, y_i^{Meas} is the measured value, and $\bar{y}^{\text{Meas}}$ is the average of all measured values. Data processing and ML approach were implemented on the Matlab platform. ML models were trained using a GPU (NVIDIA GTX 1080 Ti).

3.5. Impedance analysis

For an EIS of interest, whether it was measured or predicted, the linear K-K test method can be used to verify its rationality [46]. The EIS processing and DRT calculation were performed using a self-compiled open-source software EISART [47]. The DRT calculation is based on Tikhonov regularization (λ_0 = 0.001) and radial basis function (RBF) with prior data screening and weight assigning. The commercial software Zview was used for ECM fitting, while EISART was also used for cross-checking to ensure satisfactory fitting accuracy.

The DEIS-based method for decoupling the voltage degradation was proposed in our previous works [44,50]. The method mainly includes the following steps:

(1) EIS collection. It is necessary to collect EIS spectra at the starting time (i.e. Day 20) and the ending time (i.e. Day 217) under DC biases of 0–10 A. Here, only the EIS spectra under DC biases of 0, 5, and 10 A on Day 20 were obtained through measurements, while the remaining EIS spectra were obtained through LSTM predictions.

(2) DRT calculation. Calculate DRT corresponding to the above EIS spectra. DRT can provide a qualitative perspective on the degradation mechanisms and provide reasonable initial values for ECM fittings. In this study, the DRT calculation results can be found in Fig. 3(c) and Fig. S6.

(3) ECM fitting. The ECM used is shown in Fig. 4(a), which is informed by DRT calculation results. The fitting results of all resistances are shown in Fig. 4(b–g), and the fitting residuals are plotted in Figs. S12 and S13 for Day 20 and Day 217, respectively.

(4) Overpotential calculation. The overpotential induced by a single electrode process can be determined by the area below the corresponding resistance-current density curve in Fig. 4(b–g). Therefore, the difference between Day 20 and Day 217, i.e. the red area in Fig. 4(b–g), indicates the overpotential growth or voltage degradation caused by a single electrode process.

4. Conclusions

Data-driven modelling is a promising route for diagnostics and prognostics of electrochemical energy systems such as fuel cells. By integrating LSTM-based neural networks and DEIS analysis, we successfully predicted and decoupled the performance degradation of an industrial-sized SOFC during long-term operation. For short-term predictions of hundreds of hours, we obtained accuracies over 0.99 for both IV and EIS, demonstrating promising application prospects in diagnostics. While for long-term predictions of thousands of hours, by using the proposed approach, for the first time, the importance of each degradation mechanism—which is crucial for improving cell durability—was quantitatively determined. The performance degradation was found to be dominated by the deterioration of the anodic reaction kinetics near the TPB, followed by the deactivation of the cathodic oxygen reduction reaction and the growth of the ohmic resistance. In addition, the LSTM-based neural network shows satisfactory predictive ability in both time and frequency domains, which provides the possibility to reduce the time cost of EIS testing by more than half.

In general, present approach can complement diagnostic and prognostics approaches based on physical and semi-empirical models. Compared with conventional time-consuming tests and existing models, present approach is capable of predicting future electrochemical properties including IV and EIS, thus having the advantages of low cost and rich information. However, as a data-driven approach, the quantity and quality of data directly affect the prediction accuracy. The current data are still insufficient for predictions towards diverse cells/stacks or conditions, and therefore it is necessary to accelerate the construction of operation databases for future development of feature-rich data-driven tools.

Declaration of competing interest

The authors declare that they have no known competing financial interests or personal relationships that could have appeared to influence the work reported in this paper.

Acknowledgments

leagues in UTokyo FES lab, Tsinghua SOFC lab, and Huatsing Energy group for technical assistance and fruitful discussions.

Appendix A. Supplementary material

References

[1] S. Park, J.M. Vohs, R.J. Gorte, Nature 404 (2000) 265–267.
[2] E.D. Wachsman, K.T. Lee, Science 334 (2011) 935–939.
[3] C. Duan, R. Kee, H. Zhu, N. Sullivan, L. Zhu, L. Bian, D. Jennings, R. O'Hayre, Nat. Energy 4 (2019) 230–240.
[4] P. Boldrin, N.P. Brandon, Nat. Catal. 2 (2019) 571–577.
[5] M.M. Whiston, I.M.L. Azevedo, S. Litster, C. Samaras, K.S. Whitefoot, J.F. Whitacre, Joule 3 (2019) 2060–2065.
[6] H. Yokokawa, M. Suzuki, M. Yoda, T. Suto, K. Tomida, K. Hiwatashi, M. Shimazu, A. Kawakami, H. Sumi, M. Ohmori, T. Ryu, N. Mori, M. Iha, S. Yatsuzuka, K. Yamaji, H. Kishimoto, K. Develos-Bagarinao, T. Shimonosono, K. Sasaki, S. Taniguchi, T. Kawada, M. Muramatsu, K. Terada, K. Eguchi, T. Matsui, H. Iwai, M. Kishimoto, N. Shikazono, Y. Mugikura, T. Yamamoto, M. Yoshikawa, K. Yasumoto, K. Asano, Y. Matsuzaki, K. Sato, T. Somekawa, Fuel Cells 19 (2019) 311–339.
[7] J.T.S. Irvine, D. Neagu, M.C. Verbraeken, C. Chatzichristodoulou, C. Graves, M.B. Mogensen, Nat. Energy 1 (2016) 15014.
[8] M.B. Mogensen, M. Chen, H.L. Frandsen, C. Graves, A. Hauch, P.V. Hendriksen, T. Jacobsen, S.H. Jensen, T.L. Skafte, X. Sun, Fuel Cells 21 (2021) (fuce.202100072).
[9] Y. Zhang, B. Chen, D. Guan, M. Xu, R. Ran, M. Ni, W. Zhou, R. O'Hayre, Z. Shao, Nature 591 (2021) 246–251.
[10] S. Choi, C.J. Kucharczyk, Y. Liang, X. Zhang, I. Takeuchi, H.-I. Ji, S.M. Haile, Nat. Energy 3 (2018) 202–210.
[11] Y. Chen, B. deGlee, Y. Tang, Z. Wang, B. Zhao, Y. Wei, L. Zhang, S. Yoo, K. Pei, J.H. Kim, Y. Ding, P. Hu, F.F. Tao, M. Liu, Nat. Energy 3 (2018) 1042–1050.
[12] M. Machado, F. Baiutti, L. Bernadet, A. Morata, M. Nuñez, J.P. Ouweltjes, F.C. Fonseca, M. Torrell, A. Tarancón, J. Mater. Chem. A 10 (2022) 17317–17325.
[13] S. Pirou, B. Talic, K. Brodersen, A. Hauch, H.L. Frandsen, T.L. Skafte, Å.H. Persson, J.V.T. Høgh, H. Henriksen, M. Navasa, X.-Y. Miao, X. Georgolamprou, S.P.V. Foghmoes, P.V. Hendriksen, E.R. Nielsen, J. Nielsen, A.C. Wulff, S.H. Jensen, P. Zielke, A. Hagen, Nat. Commun. 13 (2022) 1263.
[14] H. Jeong, C. Lee, J.-W. Son, S.Y. Lee, K.J. Yoon, D. Shin, M. Choi, S.S. Shin, H. Kim, J. Mater. Chem. A 11 (2023) 7415–7421.
[15] Z. Gao, L.V. Mogni, E.C. Miller, J.G. Railsback, S.A. Barnett, Energ. Environ. Sci. 9 (2016) 1602–1644.
[16] Y. Yang, Y. Zhang, M. Yan, Sep. Purif. Technol. 298 (2022).
[17] S. Hwang, J. Lee, G. Kang, M. Choi, S.J. Kim, W. Lee, D. Byun, J. Mater. Chem. A 9 (2021) 11683–11690.
[18] N.H. Menzler, D. Sebold, Y.J. Sohn, S. Zischke, J. Power Sources 478 (2020).
[19] Q. Fang, L. Blum, D. Stolten, J. Electrochem. Soc. 166 (2019) F1320–F1325.
[20] A. Nakajo, P. Tanasini, S. Diethelm, J. Van herle, D. Favrat, J. Electrochem. Soc. 158 (2011) B1102.
[21] M.Z. Khan, M.T. Mehran, R.H. Song, J.W. Lee, S.B. Lee, T.H. Lim, J. Power Sources 391 (2018) 94–105.
[22] M. Gallo, P. Polverino, J. Mougin, B. Morel, C. Pianese, Appl. Energy 279 (2020).
[23] Y. Wang, C. Wu, Q. Du, M. Ni, K. Jiao, B. Zu, Appl. Energy Combust. Sci. 5 (2021).
[24] F. Xue, Y. Lei, T.-L. Cheng, W.K. Epting, G. Hackett, H. Abernathy, Y.-H. Wen, Int. J. Hydrogen Energy 48 (2023) 9845–9860.
[25] Y. Su, Z. Zhong, Z. Jiao, Energ. Environ. Sci. 15 (2022) 2410–2424.
[26] F. Monaco, M. Hubert, J. Vulliet, J.P. Ouweltjes, D. Montinaro, P. Cloetens, P. Piccardo, F. Lefebvre-Joud, J. Laurencin, J. Electrochem. Soc. 166 (2019) F1229–F1242.
[27] S. Zhai, H. Xie, P. Cui, D. Guan, J. Wang, S. Zhao, B. Chen, Y. Song, Z. Shao, M. Ni, Nat. Energy 7 (2022) 866–875.
[28] A. Sciazko, Y. Komatsu, A. Nakamura, Z. Ouyang, T. Hara, N. Shikazono, Chem. Eng. J. 460 (2023).
[29] V. Subotić, M. Eibl, C. Hochenauer, Energy Convers. Manag. 230 (2021).
[30] L. Xia, A. Khosravi, M. Han, L. Sun, Int. J. Hydrogen Energy (2023).
[31] J. Peng, J. Huang, C. Jiang, Y.-W. Xu, X.-L. Wu, X. Li, IEEE Trans. Transp. Electrif. 8 (2022) 4583–4594.
[32] D. Marra, M. Sorrentino, C. Pianese, B. Iwanschitz, J. Power Sources 241 (2013) 320–329.
[33] B. Dolenc, P. Boškoski, M. Stepančič, A. Pohjoranta, D. Juričić, Energy Convers. Manage. 148 (2017) 993–1002.
[34] M. Li, J. Wu, Z. Chen, J. Dong, Z. Peng, K. Xiong, M. Rao, C. Chen, X. Li, Energies 15 (2022).
[35] W. Ming, P. Sun, Z. Zhang, W. Qiu, J. Du, X. Li, Y. Zhang, G. Zhang, K. Liu, Y. Wang, X. Guo, Int. J. Hydrogen Energy 48 (2023) 5197–5228.
[36] S. Wang, J. Zhang, O. Gharbi, V. Vivier, M. Gao, M.E. Orazem, Nat. Rev. Methods Prim. 1 (2021) 41.
[37] S. Dierickx, A. Weber, E. Ivers-Tiffée, Electrochim. Acta 355 (2020).
[38] B.A. Boukamp, A. Rolle, Solid State Ion. 314 (2018) 103–111.
[39] Y. Zhang, Q. Tang, Y. Zhang, J. Wang, U. Stimming, A.A. Lee, Nat. Commun. 11 (2020) 1706.
[40] E. Quattrocchi, B. Py, A. Maradesa, Q. Meyer, C. Zhao, F. Ciucci, Electrochim. Acta 439 (2023).
[41] K. Yang, J. Liu, Y. Wang, X. Shi, J. Wang, Q. Lu, F. Ciucci, Z. Yang, J. Mater. Chem. A 10 (2022) 23683–23690.
[42] X. Liu, Z. Yan, J. Wu, J. Huang, Y. Zheng, N.P. Sullivan, R. O'Hayre, Z. Zhong, Z. Pan, J. Energy Chem. 78 (2023) 582–588.
[43] G.T. Le, L. Mastropasqua, J. Brouwer, S.B. Adler, J. Electrochem. Soc. 169 (2022).
[44] Z. Lyu, H. Li, M. Han, Z. Sun, K. Sun, J. Power Sources 538 (2022).
[45] G. Van Houdt, C. Mosquera, G. Nápoles, Artif. Intell. Rev. 53 (2020) 5929–5955.
[46] M. Schönleber, D. Klotz, E. Ivers-Tiffée, Electrochim. Acta 131 (2014) 20–27.
[47] H. Li, Z. Lyu, M. Han, Electrochim. Acta 422 (2022).
[48] K. Chen, S.P. Jiang, Electrochem. Energy Rev. 3 (2020) 730–765.
[49] X. Guo, R. Waser, Prog. Mater Sci. 51 (2006) 151–210.
[50] Z. Lyu, S. Liu, Y. Wang, H. Li, Z. Liu, Z. Sun, K. Sun, S. Zhang, M. Han, J. Power Sources 510 (2021).
[51] R. Xiong, J. Tian, W. Shen, J. Lu, F. Sun, J. Energy Chem. 76 (2023) 404–413.
[52] Y. Lu, C.-Z. Zhao, J.-Q. Huang, Q. Zhang, Joule 6 (2022) 1172–1198.
[53] W. Hu, Y. Peng, Y. Wei, Y. Yang, J. Phys. Chem. C 127 (2023) 4465–4495.